CFD Analysis in Development of Flight Test Article for Basic Research

Datta V. Gaitonde[*], **Roger L. Kimmel**[†], **Dwayne Jackson**[‡]
Air Vehicles Directorate
Air Force Research Laboratory
Wright-Patterson AFB, OH

Xiaolin Zhong[§]
Mech. and Aerosp. Eng. Dept.
University of California (UCLA)
Los Angeles, CA

Abstract

A broad computational fluid dynamics (CFD) based effort is described to guide development of a flight test article for exploration of fundamental high-speed fluid dynamic phenomena which affect thermo-mechanical loading and mass capture. The specific focus is on obtaining data on natural transition to turbulence over a sphere-cone configuration, as well subsequent strong (separated) shock/turbulent boundary layer interactions associated with a cylinder/flare juncture. The experiment also includes the option of an integrated channel to mimic internal flow in which the survivability and performance of instrumentation to measure mass capture metrics may be evaluated. This aspect, together with the expected inclination of the flight vehicle to the freestream, introduces the need for fully 3-D analyses. Uncertainty and risk reduction are addressed by employing different codes, freestream conditions (Mach and Reynolds numbers, angles of attack and side-slip), wall thermal conditions, model fidelity (invicid, laminar and multiple turbulence models), potential real gas effects, and stability analyses. Preliminary comparisons with concurrent complementary ground-test data are described: post-flight analyses will aid in identification of crucial differences between the flight and ground test environments.

I. Introduction

The quest for routine and sustained hypersonic flight requires considerable additional understanding and control of key phenomena. The complexity of the flow field, and consequent impact on thermo-mechanical loads as well as propulsion efficiency, arises from several factors. In addition to shock waves, new mechanisms of compressible transition can arise over and above those encountered at low speeds. Subsequent turbulent boundary layer interactions can often yield unsteady and three-dimensional vortical structures, separation and reattachment. Under suitable conditions, the high-temperatures encountered can excite multiple internal energy modes which interact with each other in chemical non-equilibrium.

The tools employed to understand hypersonic flight include computational simulations and ground and flight testing. Each approach has inherent strengths and limitations. For phenomena involving transition and turbulence, techniques based on direct numerical simulations have proven to be relatively difficult and expensive because of the need to resolve a broad spectrum of spatio-temporal scales, and inadequate knowledge of the noise environment. Similarly ground-test facilities often cannot reproduce flight parameters to sufficient fidelity. This is particularly true when transition is a major factor, since the noise environment in ground-test is generated by tunnel wall boundary layers. High enthalpies and short test run times at flight parameters are also an issue. Flight testing is expensive and though representative of the desired conditions, is often very difficult to characterize, in terms of freestream determination and uncertainties associated with *in situ* diagnostic device performance and survivability. It is evident that the most efficient approach to resolving these complex issues is to combine computational, ground and flight-test in a synergistic manner. The focus of this paper is on the first of these thrusts.

[*] Tech Area Leader, Associate Fellow, AIAA
[†] Research Engineer, Associate Fellow, AIAA
[‡] Research Engineer, Member, AIAA
[§] Professor, Associate Fellow, AIAA

The current flight test experiment has three main goals, each of which addresses a major deficiency in current knowledge. The primary experiment is designed to examine natural transition of a boundary layer over a blunted cone configuration in the relatively low-noise flight environment. The secondary objective is to obtain data in a (turbulent) shock/boundary layer interaction associated with a downstream flare. To optimize data acquisition, and to lay the groundwork for a future test on internal flow measurements, a tertiary experiment is incorporated to examine performance and survivability of a mass-capture measurement device. This is facilitated by insertion of a channel in the flare section to provide a pseudo-internal flow. The trajectory is assumed to be similar to that of the HYSHOT II, utilizing a two-stage Terrier-Orion launch vehicle. The vehicle reaches an apogee of about 300km, with test data acquisition possible during both ascent (supersonic) and descent (hypersonic) between 23km and 37km. Additional information on the flight path may be found in Ref. 1.

Numerical simulations to optimize flight test article development span a wide range of tools and techniques, from empirical and semi-empirical approaches to full 3-D simulations with the Navier-Stokes equations. In the context of the current experimental plan, a framework has been established to employ various levels of approximations, but the focus of the current paper is on higher-fidelity CFD. Specifically, numerous simulations addressing different dimensions of the problem are described. These employ a range of theoretical models, including inviscid, laminar and turbulent governing equations. A preliminary assessment of potential high-temperature effects is also performed. To reduce computational load, the assumption of an axisymmetric flow is invoked where possible, but full three-dimensional simulations are also undertaken when necessary. Other papers to be published (*e.g.,* Ref. 2) will describe specific measurements to be acquired, the design of suitable gauges and data transfer requirements - for these aspects, only some preliminary considerations are presented here in the context of the CFD thrust.

Several different codes are employed, including AVUS,[3] FDL3DI,[4] GASP[5] and Cart3D.[6] Brief descriptions of each are provided where appropriate. Comparisons are drawn where possible to subset canonical configurations, for which prior highly resolved calculations have yielded detail insight.

- Since the conditions are likely to vary over the flight envelope where data is acquired, the simulations consider different nominal freestream parameters, with emphasis on Mach 6.5 and 7.5 regimes.
- Both laminar and turbulent conditions are simulated since each regime is likely to be encountered in different segments of the flight path. The two flow states effectively bound the flow environment. For turbulent flow, models chosen reflect mature components of the specific code employed.
- Based partly on the above simulations, the designed test vehicle has recently been subjected to ground-test experiments. Preliminary comparisons with these results are summarized.
- Separate simulations are performed with non-equilibrium chemistry and thermal mode excitation to examine the extent of high-temperature effects under the chosen conditions.
- An initial examination of the stability of the entropy layer has been performed
- To generate force data under parameteric variation of angle of attack and sideslip, inviscid 3-D simulations are generated with a fast Cartesian-based approach. Preliminary viscous 3-D simulations at nominal 2^o sideslip are summarized.
- Finally, full 3-D viscous laminar and turbulent analyses of the vehicle with channel cutouts are described on a hybrid mesh.

II. Evolution of configuration design

Figure 1 depicts the main milestones in the evolution to the final design of the test article. The basic configuration, suited for transition data acquisition is shown in Fig. 1a and consists of a simple sphere-cone combination. To build on prior experimental and computational experience,[7,8] the cone half angle is fixed at 7 degrees. The nose radius is nominally fixed at $2.5mm$, to maintain a manageable nose-tip heat load, while also yielding a high likelihood of transition occurring during the flight path where data will be acquired. For the secondary shock/boundary layer interaction, a 37^o flare is appended as shown in Fig. 1b. This angle assures a separated flow even when the flow is fully turbulent as based upon results from preliminary empirical considerations and turbulent simulations. Subsequent ground-test data suggest however that a 33^o-degree flare is a more suitable choice, in that the separating shear layer reattaches on the flare face at nominal conditions. In this effort however, all calculations below employ the 37^o flare (results with the 33^o flare face are currently in progress, and will be presented in a subsequent report).

Simulations on the configuration of Fig. 1b reveal a relatively large upstream influence of the flare, suggesting the possibility of undesirable shock-induced transition instead of natural sequence originating in the receptivity mechanism. To preclude this, an isolator segment is added between the cone and the flare. Simulations and recent complementary ground tests suggest that the shoulder expansion does not laminarize the boundary layer, thus separating the transition and turbulent shock/boundary layer interaction components of the experiment. The final configuration, Fig. 1d, includes two symmetric channels (Fig. 1e) providing pseudo-internal paths across which laser-based data may be acquired. The dimensions employed in the calculations are as follows. The flare/isolator juncture lies $1m$ from the nose, while the isolator cylindrical segment is $0.6m$. Mating considerations with the motor limit the base diameter - this yields a relatively short flare segment of $5cm$. The simulations consider a total length of $1.8m$, facilitating examination of the asymptotic state after the flare shoulder expansion. The radius of the isolator is $0.137m$, while that of the base is $0.178m$.

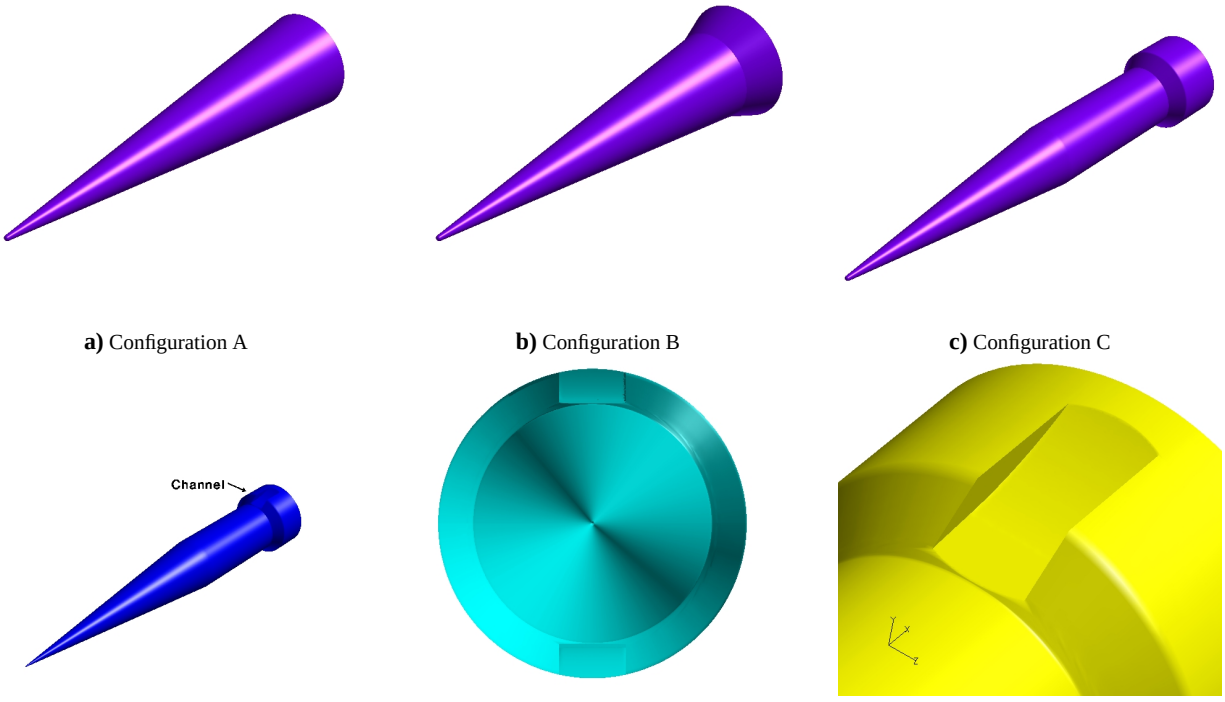

a) Configuration A **b)** Configuration B **c)** Configuration C

d) Configuration D **e)** Configuration D - Channel Placement **f)** Configuration D - Channel Close-up

Figure 1. Evolution of configuration

III. Axisymmetric flow

The nominal case considers a Mach number of 7.5 and a Reynolds number, Re of 2.3×10^6 based on length of $1.8m$. The freestream temperature T_∞ is taken to be $236.51K$ and the freestream static pressure p_∞ is $574.6Pa$. Subsequently, the flow at a lower Mach Number of 6.5, $T_\infty = 225.56K$ and $p_\infty = 9289.46$ respectively is simulated. Finally, the parameters corresponding to one of several recent ground tests (Run 5) are considered, consisting of $M = 7.16$, $Re = 1.8 \times 10^7$, $T_\infty = 231.67K$ and $p_\infty = 4620N/m^2$.

As noted earlier, several different codes have been employed to examine different aspects of the flowfield. The broad features obtained for all viscous simulations are similar and are described first. Several meshes are employed for the different configurations of Fig. 1. Results described here focus on Configurations C and D. The structure of meshes employed for axisymmetric calculations performed on Configuration C is shown in Fig. 2. A typical mesh consists of about 600 points in the streamwise direction, 100 points normal to the body and 5 planes in the azimuthal direction to facilitate imposition of axisymmetric conditions. All meshes are clustered near the surface, as well as in the vicinity of the shock/turbulent boundary layer interaction.

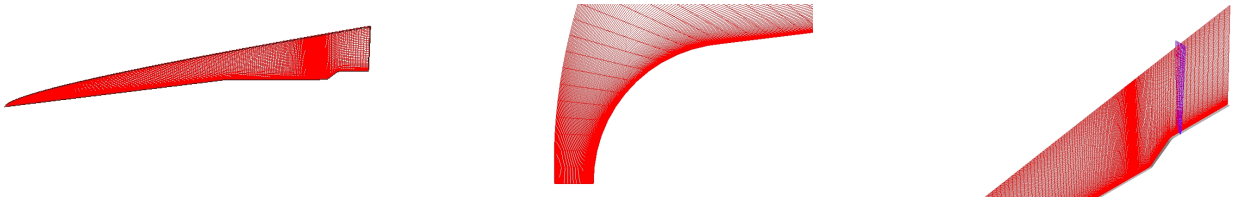

a) Overview **b)** Nose region **c)** Flare region

Figure 2. Mesh structure for axisymmetric cases - not all points shown

A. Features of baseline flowfield

Figures 3a and b depict the overall Mach and pressure patterns, the latter normalized by freestream dynamic pressure. The main features are the strong bow shock in the nose region and the shock/boundary layer interaction downstream. Details of the former are shown in Figs. 3c and d respectively. The highest heating and pressure occur at the stagnation point on the nose. The flow expands around the sphere to yield a relatively slowly evolving boundary layer on the cone, where transition is anticipated to occur. In this laminar case, the flow separates near the shoulder comprised by the cone/cylinder (isolator) juncture because of the upstream influence of the flare shock. Aspects of the flow structure within the separated region are shown in Figs. 3e through h. The main feature is the development of a complex separated region comprised of several cells of recirculating fluid. A key aspect is the observation of unsteadiness, reflected in changes in the size of the cells, and the shock intersection with the flare surface. Details of the transients have not been studied extensively, since the absence of three-dimensionality in the present calculations precludes the development of transition to turbulence.

Although the three viscous codes employed, *AVUS*, *FDL3DI* and *GASP* all show the same general features shown in Fig. 3, details of the shock boundary layer interaction differ both in terms of the unsteady features, as well as the location of flow reattachment at the flare/base intersection, from which emanates an expansion. In particular, the location of reattachment of the separated shear layer varies significantly, as do the local peaks in heat transfer and surface pressure. When reattachment occurs near the flare/base juncture, the impact of the trailing expansion becomes more prominent as expected.

Figure 4 depicts the surface pressure and heat transfer rates for the actual and extended flare configurations. High values are observed at the nose as anticipated. In this region, Fig. 4b, both designs indicate very similar values since the impact of the flare is only observed further downstream. However, the extent of the interaction is significantly lower when the flare shock is muted by the shoulder, thus ensuring the effectiveness of the cylindrical isolator even in the laminar case characterized by large upstream influence. In the flare region, Fig. 4c, both pressure and heat transfer are muted by the flare/base shoulder expansion while they rise monotonically in the extended flare case.

B. Effect of Flow Parameters

As noted earlier, the flight path of the vehicle spans a range of freestream parameters. To examine the effect of this variation, simulations were performed for two different conditions, Mach 7.5 and 6.5 noted earlier. Figure 5a exhibits the Mach number variation along the stagnation streamline. The shock standoff distance, measured as the point where the flow becomes sonic, is slightly larger for the lower Mach case. Moreover, the results, $\delta/D \sim 0.07$ are in good agreement with those provided in the literature.[9] Examination of the surface loading parameters (Figs. 5b through d), suggests that the normalized pressure is marginally higher at $M = 7.5$. However, the unnormalized heat transfer rate of practical interest is larger at $M = 6.5$. Stagnation point heat transfer values may be compared with the Fay and Riddell theory.[10] Even on these relatively coarser meshes, the stagnation heat transfer is captured to within roughly 5 percent of the anticipated value, which is higher at Mach 6.5, because of the different freestream enthalpy. The undulations in surface loading in the flare region, are consistent with an unsteady regime that cannot be resolved with the present axisymmetric assumption, since the breakdown to turbulence requires resolution of azimuthal disturbance growth. Further studies are currently in progress to address the issue of unsteadiness in this interaction.

C. Effect of wall temperature

The sensitivity of laminar flow to modest variations of wall temperature anticipated during the data acquisition phase is examined in Fig. 6, which exhibits surface loading variaton for a $100K$ change in surface temperature. No significant flow field differences are discernable, though ongoing stability calculations may suggest an influence on the location

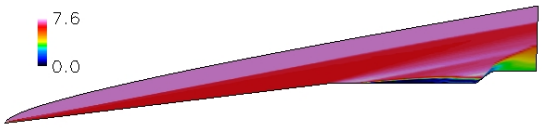

a) Mach contours

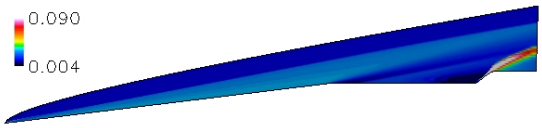

b) Pressure contours

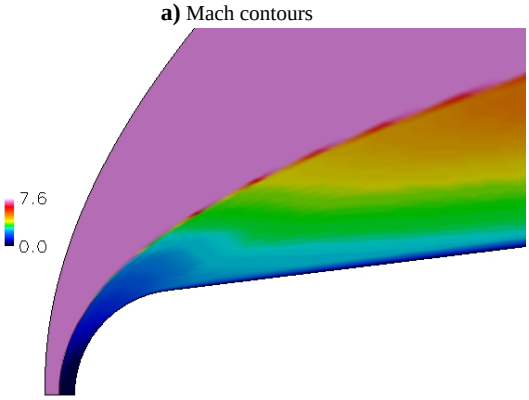

c) Mach nose region

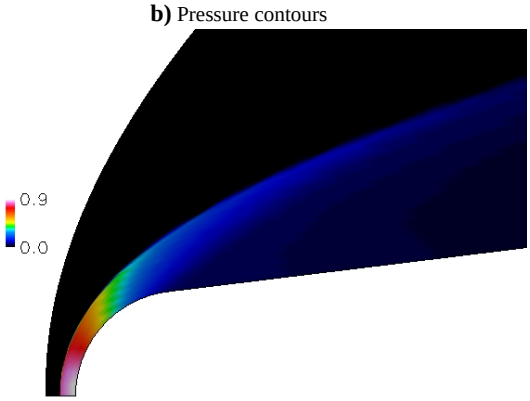

d) Pressure nose region

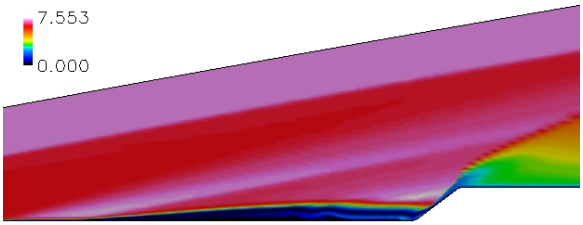

e) Mach flare region

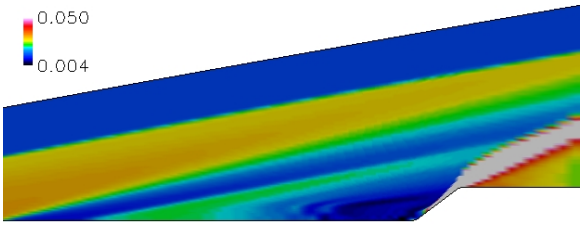

f) Pressure flare region

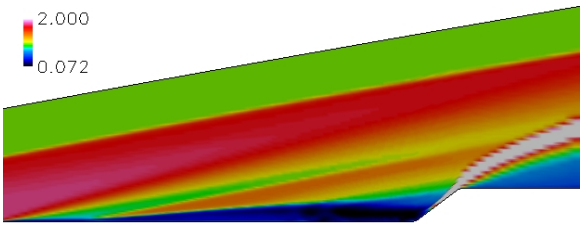

g) Density flare region

h) Streamlines in SBLI

Figure 3. Aspects of baseline flow field

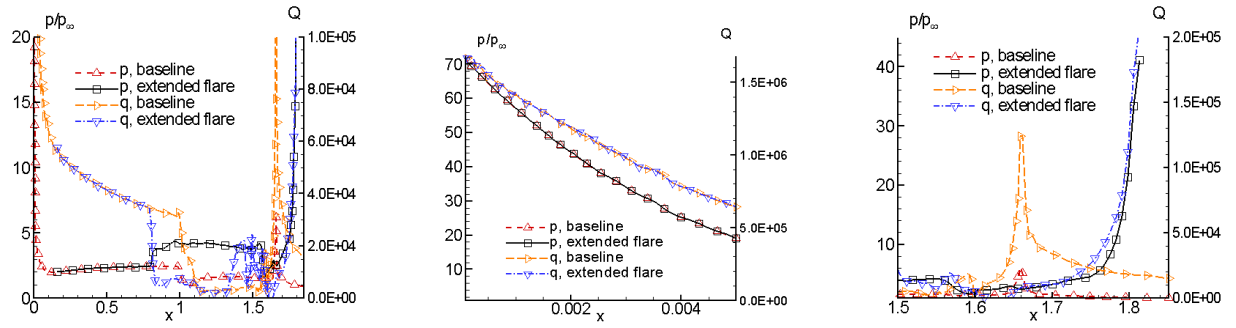

a) Overview **b)** Nose region **c)** Flare region

Figure 4. Surface loading parameters for baseline case

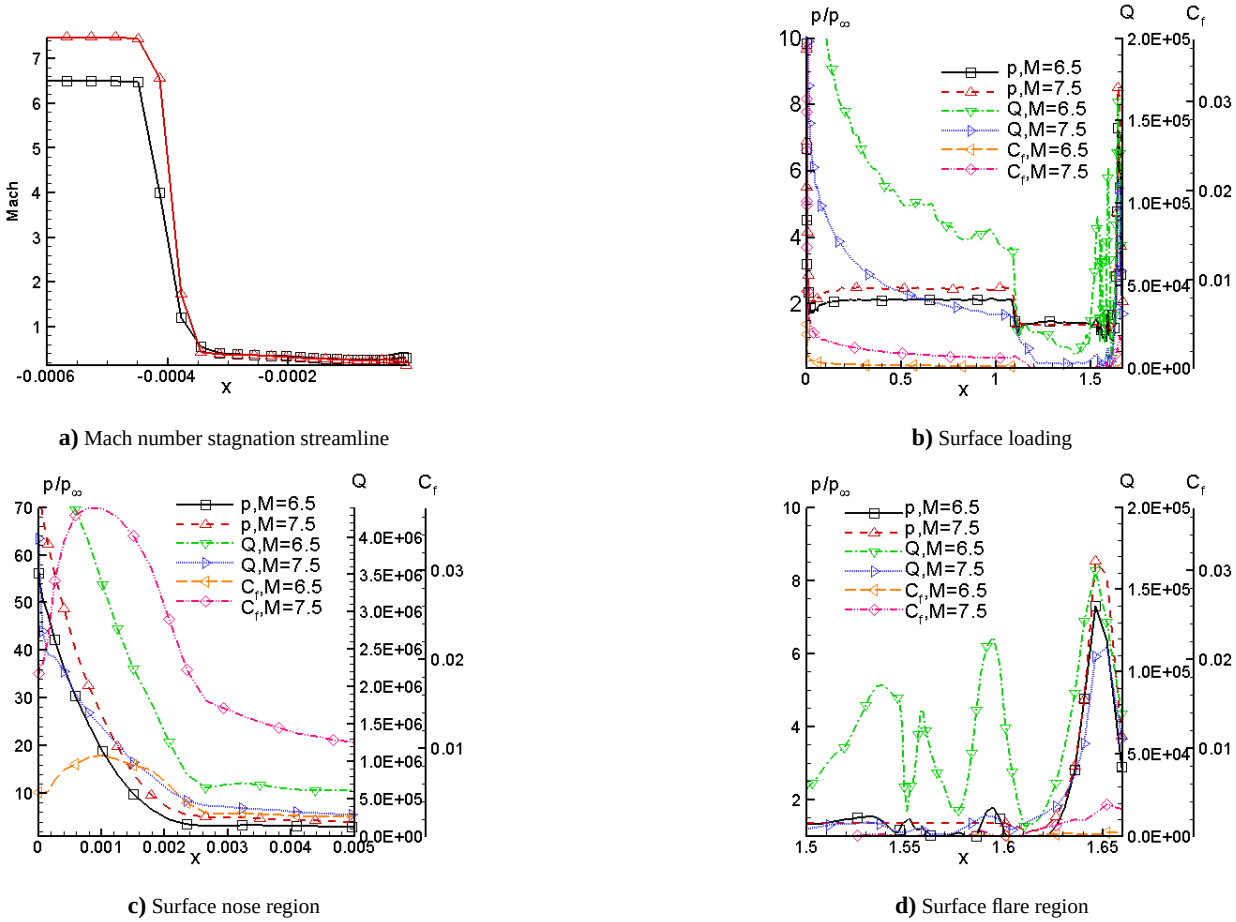

a) Mach number stagnation streamline **b)** Surface loading

c) Surface nose region **d)** Surface flare region

Figure 5. Effect of flight parameter

of transition (see § E below). In the nose region, the most sensitive parameter is the skin friction coefficient, where the higher temperature yields a more rapid growth, possibly as a result of higher local viscosity. In the flare region downstream, the heat transfer rate exhibits a similar increase.

An exploratory study has also been conducted to discern high-temperature effects on the flow field. For this purpose, the commercial software GASP, which includes several thermo-chemical non-equilibrium models is employed. The particular model chosen is the "Park 1" variant, consisting of 5 species (N_2, O_2, O, NO and N) coupled through 17 reactions. Figure 7 exhibits Mach contours of the region near the flare interaction. Comparison with earlier results without high temperature effects indicates that the main features are similar to those obtained with perfect gas assumptions. Thus, within the constraints of this model, high-temperature effects are not significant. Even under adiabatic catalytic wall conditions, chosen so that the surface temperature is near the higher bound of possible variation, the degree of dissociation is found to be negligible. However, under these conditions, vibrational excitation is potentially a significant effect. To resolve this, simulations with a single vibrational temperature, T_v, representing the vibrational

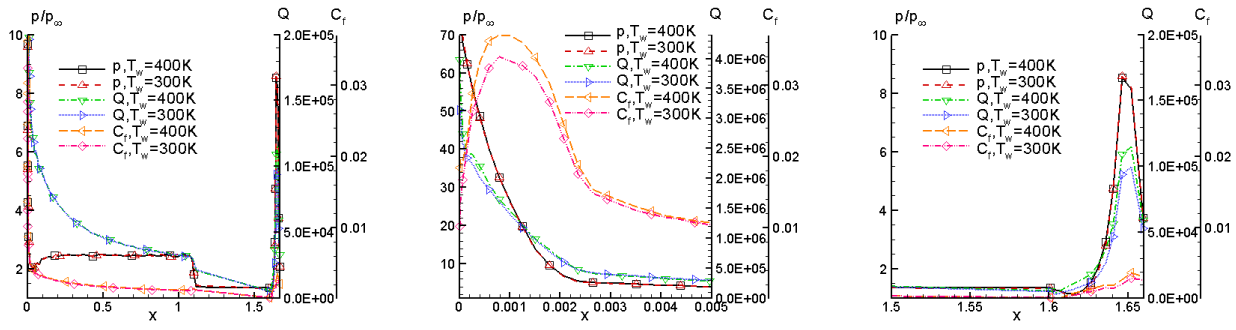

a) Overview **b)** Nose region **c)** Flare region

Figure 6. Effect of wall temperature on surface loading

state of molecular components have been completed. Results along the stagnation streamline are shown in Fig. 7c. Several observations may be readily made. The shock standoff distance is significantly diminished, consistent with the theory. A key effect downstream of the shock is the gradual excitation of the vibrational energy mode, which reaches equilibrium with the translational mode at the surface, as follows from the imposed boundary conditions. The wall thermal and catalyticity conditions have an important effect on these results, both of which are currently being investigated.

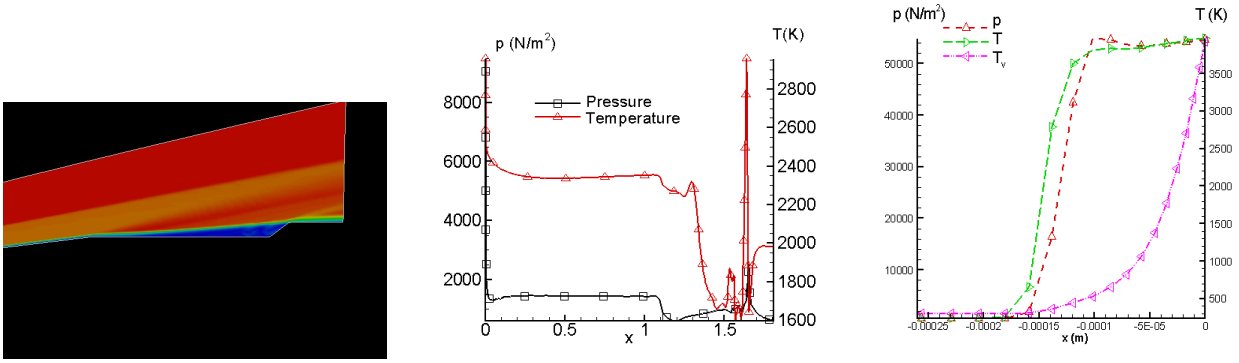

a) Mach contours **b)** Surface loads - single T model **c)** Stagnation streamline - $T - T_v$ model

Figure 7. Preliminary assessment of high-temperature effects

D. Preliminary comparisons with ground test data

As noted earlier, a complementary ground test effort has been undertaken at CALSPAN to guide the final development of the test article. Some preliminary results, provided by Holden and Wadhams,[11] are employed to initiate a systematic validation effort. The data include pressure and heat transfer rates in the cone and cylinder segments, and flow visualization of the cylinder/flare juncture. Of the many cases, here Run 5 is considered, parameters for which have been noted earlier. These simulations were performed with the FDL3DI code which includes the two-equation $k - \epsilon$ model,[12] together with a compressibility correction.[13] Further details of the numerical methodology may be found in Ref. 14.

Figure 8a compares the surface pressure, normalized by the freestream dynamic pressure, to experimental values. The results from both laminar and turbulent simulations are plotted. It is evident that both results predict the pressure accurately upstream of the cone/cylinder intersection. Downstream however, the laminar results exhibits rapid rise, consistent with a large upstream influence of the flare as discussed previously. The turbulent simulation predicts the reduction across the juncture accurately, with the pressure reaching a relatively constant value on the cylinder before the rise associated with the shock/boundary layer interaction.

Figure 8b shows the schlieren image obtained in the experiment. Turbulent results with the default model are shown in Figs. 8c and d, which show the magnitude of the density gradient and the u velocity respectively. Scrutiny of the figures suggests that while both show separation, the computed extent is smaller. Partly as a consequence, the separated shear layer in the computation appears to impinge on the flare surface, in contrast to the situation in the experiment. Several possibilities exist to account for these discrepancies, which are being examined in present work. In general RANS approaches have not yielded accurate SBLI results,[15] without suitable optimization for each problem

of interest. Even variants within a given turbulence model can have a significant impact on complex shock/boundary layer interactions. For example, Figure 8e and f show results when the compressibility correction, which is usually beneficial in separated but not attached flows, is switched off. The flow in this case does not exhibit the large separation region, and resembles those obtained with the unoptimized Spalart-Allmaras model (not shown). Current effort is focused on addressing this issue as well as others related to mesh resolution, which, given the exploratory nature of these simulations, is presently not adequate to resolve details of this sub-experiment. Other ongoing tasks include fixing transition location at about the same point as in experiment (about $0.4m$ from the nose), exploration of the effect of freestream turbulence (chosen to be 0.5% here) and the relaminarization effect of the cone/cylinder juncture, which may yield a larger separation zone.

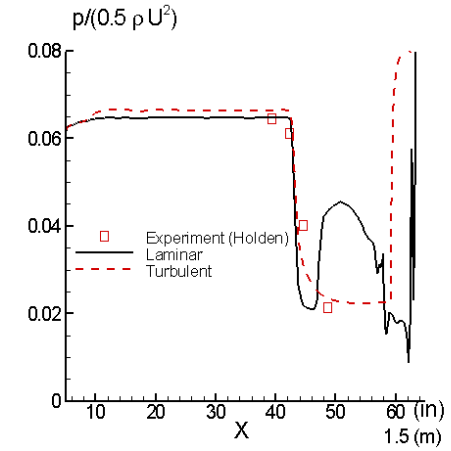

a) Surface pressure

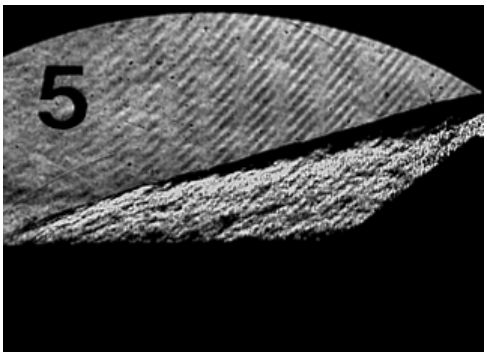

b) Expermental visualization of separated flow (from Holden, CALSPAN)

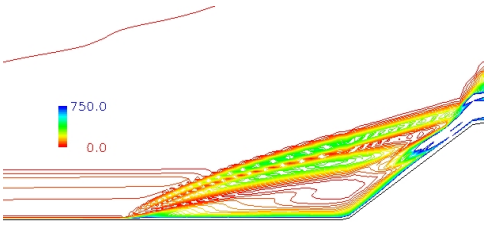

c) With CC: $|\bigtriangledown \rho|$

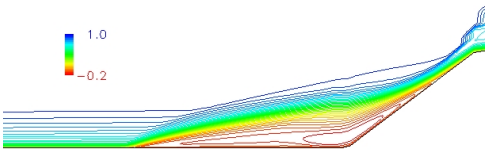

d) With CC: u

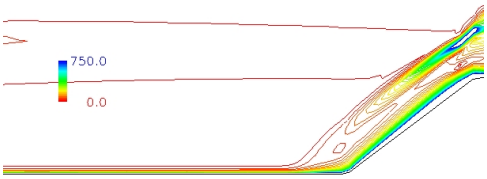

e) Without CC: $|\bigtriangledown \rho|$

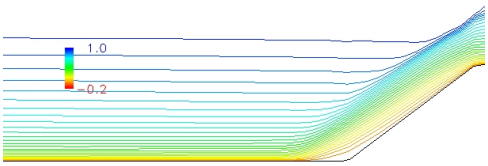

f) Without CC: u

Figure 8. Preliminary comparison with experimental data, CC=compressibility correction

E. Stability simulation and analysis

The mechanism of natural transition is extremely complex, following a path in which freestream disturbances initially morph into unstable modes through a receptivity process, followed by linear growth and subsequent breakdown. Further, unlike in the subsonic case, multiple instability modes occur at hypersonic Mach numbers.[16–18] Surface

roughness can have a profound impact on this development, especially near the nose where the boundary layer is thin, placing limitations on the location of joints and degree of polish. Wind tunnel tests[19] also indicate the importance of the nose radius in determining the location of transition. Experimental results have shown that increasing nose bluntness delays transition. Stetson et al.[19] found evidence of inviscid entropy instability in the region outside of boundary layers for blunt cones at a Mach 8 freestream (cf. Ref. 20).

The current state of the art in predicting natural transition in hypersonic boundary layer transition is the e^n method, which is based on the relative linear growth of instability waves. Nevertheless, the e^n method suffers from a major drawback that it does not consider the effects of receptivity of the boundary layer to freestream disturbances, surface roughness, or other perturbation sources. Because of the limitations of various transition prediction techniques, a combination of flight experiments, stability analyses, and numerical simulation of boundary layer receptivity and stability will be valuable in better prediction of transition. Studies have been initiated on linear stability analysis of the mean flow solutions[21,22] and the e^n prediction method. Velocity profiles on the cone surface have been extracted as shown in Fig. 9a and employed to determine edge properties at several streamwise locations.

A summary of linear stability analyses on response of wave modes in the base flow is now presented to predict receptivity of freestream fast acoustic waves. A fifth-order shock-fitting code is used to simulate the transient response of the boundary layer to freestream perturbation waves. The specific test case in the receptivity simulation corresponds

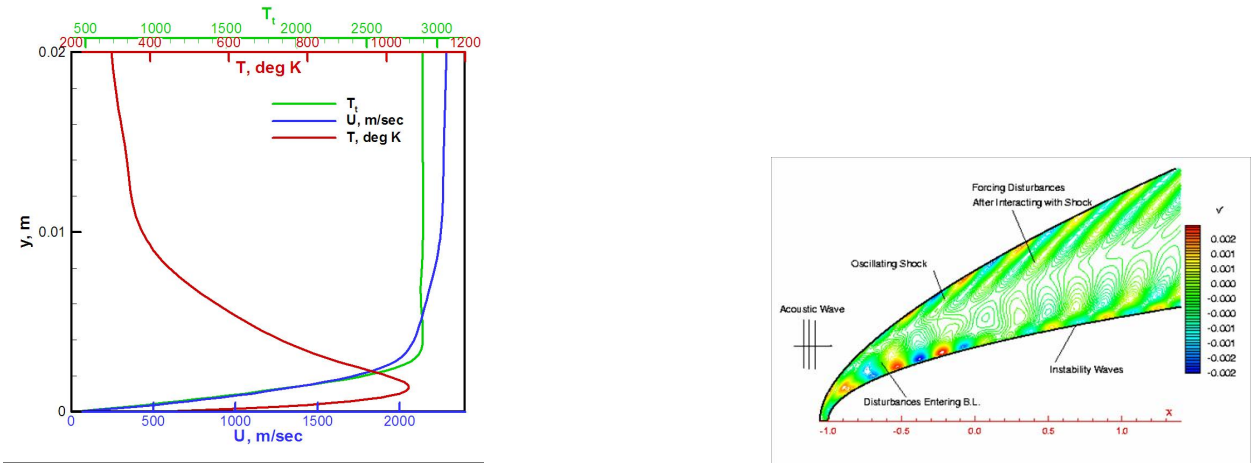

a) Profiles **b)** Acoustic pattern

Figure 9. Key profiles and acoustic response of base flow

to the Mach 6.5 parameters described earlier, with nose radius $2.5mm$ and a wall temperature of $300K$. The freestream acoustic waves are composed of a combination of 31 independent frequencies in the range $30kHz$ to $900kHz$. The relative freestream wave amplitude is 0.01%. A sample acoustic pattern obtained is depicted in Fig. 9b. Once the transient flow is computed to periodic state, instantaneous results are recorded for FFT analysis and amplitudes and phase angles of the flow perturbations are obtained.

Results for pressure amplitude variation with streamwise distance for several modes, and corresponding pressure contours at two select frequencies are shown in Fig. 10. In the figure, the x and y coordinates are nondimensionalized by the nose radius of $2.5mm$, while pressure is normalized by the freestream pressure.

Figure 10 shows pressure perturbations for a range of forcing frequencies along the cone surface. Each line in Fig. 10a and 10b represents one of the frequencies given by $F_n = 30nkHz$. The results show that the receptivity process leads to very complex induced wave structures in the boundary layer. For all frequencies, Fig. 10a and b show that the wave amplitudes first increase near the nose region due to a resonant interaction between the forcing waves and the boundary layer wave modes.[22] This initial growth is followed by a decay and subsequent wave modulation. The amplitudes will experience a substantial rapid growth downstream of the initial zone if the second mode instability waves for that frequency are excited and unstable. The exponential amplitude growth of the second mode is the main cause of natural transition in present flow environment over the blunt cones. Figure 10b shows that for the frequency of $690kHz$ ($n = 23$), the pressure amplitudes show rapid growth of the second mode approximately at $x = 240 \times 2.5mm = 0.6m$. The second mode growth for a lower frequency of $630kHz$ ($n = 21$) occurs later along the surface. This second mode growth is a direct results of the receptivity process and will be compared with a separate linear stability result in a subsequent report .

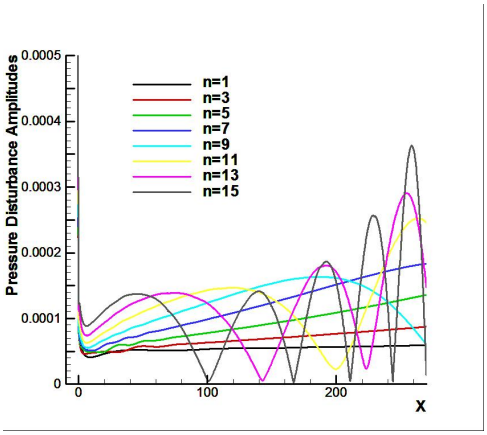

a) Lower frequency modes

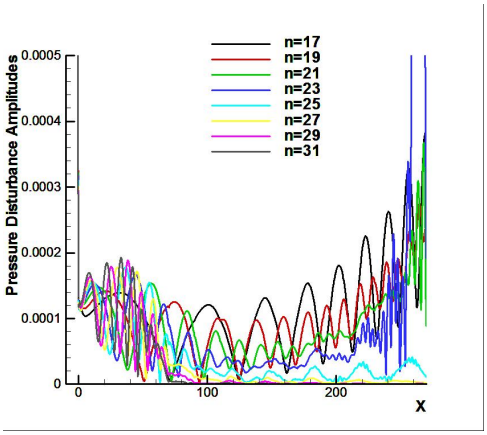

b) Higher frequency modes

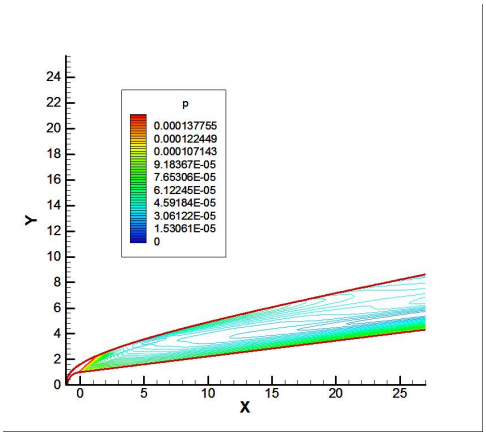

c) Pressure perturbation amplitudes at $390kHz$

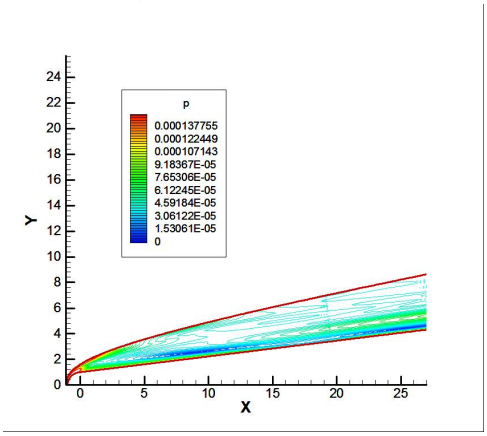

d) Pressure perturbation amplitudes at $870kHz$

Figure 10. Receptivity simulation with multi-frequency input ($F_n = 30nkHz$)

IV. 3-D simulations

The flowfield past the final configuration, Fig. 1d, is fully three-dimensional. Even without the channel, a static analysis of sideslip or angle-of-attack effects necessitated by the fact that the vehicle exhibits modest pitching and rolling motion, also requires fully 3-D analyses. Below, results from some initial simulations are presented.

A. Angle-of-attack simulations

In order to obtain integrated load data under parameteric variation of angle-of-attack, the Cart3D package is employed. The approach, based on inviscid analysis, greatly aids conceptual and preliminary aerodynamic design. A major advantage is the high degree of automation and computational efficiency. Starting from a surface triangulation, an automatic meshing process generates a Cartesian grid and provides the inviscid flow structure with force and moment information. Upwind flux evaluations are coupled to adaptive Cartesian mesh refinement with cut-cells and multi-grid Runge-Kutta time integration. Because of its high efficiency, the need to exploit symmetry is reduced, and simulations at various angles of attack and sideslip are greatly facilitated.

A typical grid and solution are shown in Fig. 11a and b respectively. The domain in which the solution is to be obtained is specified by a box surrounding the configuration. In the present case, since the base is not required, the downstream end of the domain is coincident with the base. Prespecified regions where high mesh refinement is required are identified near the nose and flare/channel regions. The procedure splits cells successively in these regions, employing the natural grid sequencing procedure to accelerate solution convergence. Figure 11b exhibits the features of a sample solution during its evolution. The main shock structures, including the nose bow shock and the flare shock are captured crisply, with no discernable oscillations. The distortion of the shock profile on the base plane, associated with the flowfield in the channel, is manifested in the form of a dimpling which brings the shock location closer to the body. Viscous simulations described below show similar behavior.

The trajectory of the reentry vehicle exhibits both roll as well as an angle of attack, and thus precession. In order

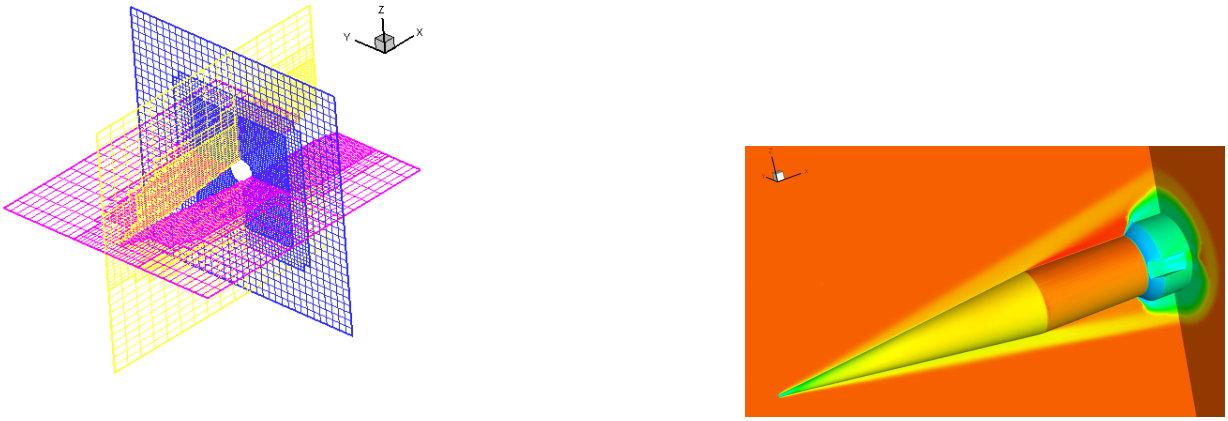

a) Cartesian mesh approach **b)** Mach contours

Figure 11. Overall features of solution obtained with Cart3D

to examine the deviation of the flow under these conditions, a preliminary parametric study has been perfomed by varying the pitch and side-slip angles from 1^o to 5^o in increments of 1^o. For brevity, only the impact on the flow in the vicinity of the channel is shown in Figure 12 with the pressure coefficient for select points in the parameter space. Figure 12a depicts the profile of the pressure variation at the nominal zero deviation angle case. The solution is symmetric about the $z = 0$ plane. High pressure values are observed on the ramp face, but the peak occurs near the trailing edge of the channel. The principal effect of pitch is to increase the magnitude and dimensions of the high Cp spot shown in Figs.12b, c and d in which the windward plane view is shown. Examination of the leeward side of the vehicle indicates that the high pressure persists, but magnitudes are muted relative to the zero deviation case. The shock associated with the flare is only modestly affected however, because of the mitigating effect of the windward channel cutout. The effect of side-slip is shown in Figs. 12e through g. In this case, the high-pressure spot successively moves towards the corner of the channel. The shock strength on the $y - z$ plane is now asymmetric, with a stronger structure on the windward side. Highest pressures tend to occur on the flare surface, since the interior of the channel is effectively shielded. Figure 12h shows the effect of simultaneous 5^o pitch and 5^o sideslip. It is evident that the combined effect is not linear in these parameters.

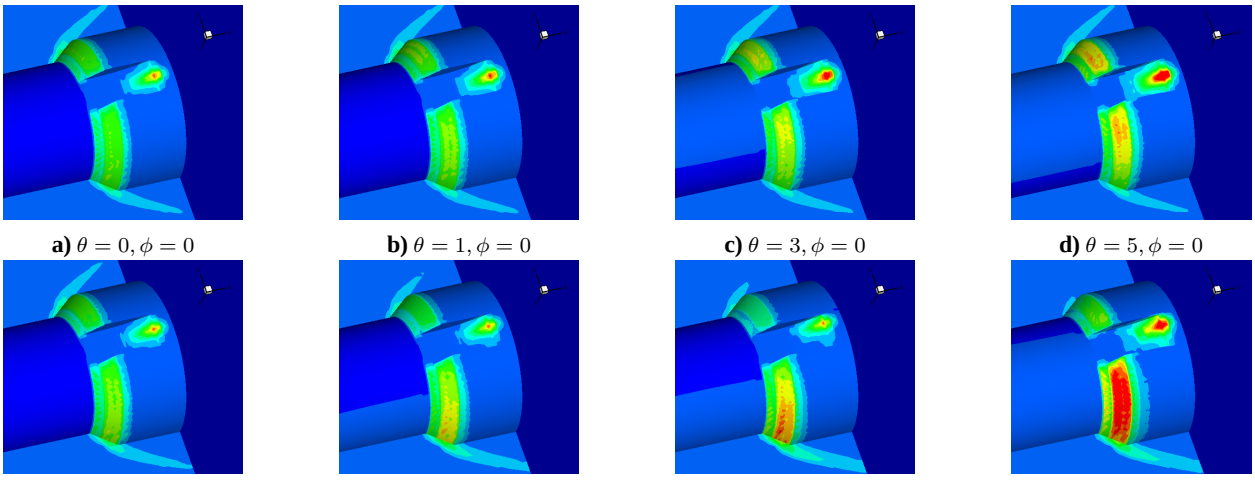

a) $\theta = 0, \phi = 0$ **b)** $\theta = 1, \phi = 0$ **c)** $\theta = 3, \phi = 0$ **d)** $\theta = 5, \phi = 0$

e) $\theta = 0, \phi = 1$ **f)** $\theta = 0, \phi = 3$ **g)** $\theta = 0, \phi = 5$ **h)** $\theta = 5, \phi = 5$

Figure 12. Effect of parameter variation on pressure coefficient near channel, θ is the pitch angle (windward side shown), ϕ is the sideslip angle

An assessment of the integrated force variation along body axes is shown in Fig. 13 separately with pitch and sideslip. The largest force is the streamwise component as anticipated. A modest monotonic but slightly non-linear increase is observed with increasing pitch. The vertical force (lift) also increases, almost linearly at a faster rate, while the side force is unaffected by pitch. The effect of side-slip is also similar, except that the side force increases rapidly, while the vertical force remains negligible because of the symmetric nature of the configuration. For this relatively long body, the effect of even small angles of attack may be significant at the downstream end of the domain.

Viscous effects under angle-of-attack have also been explored. The solver employed for these fully 3-D simulations

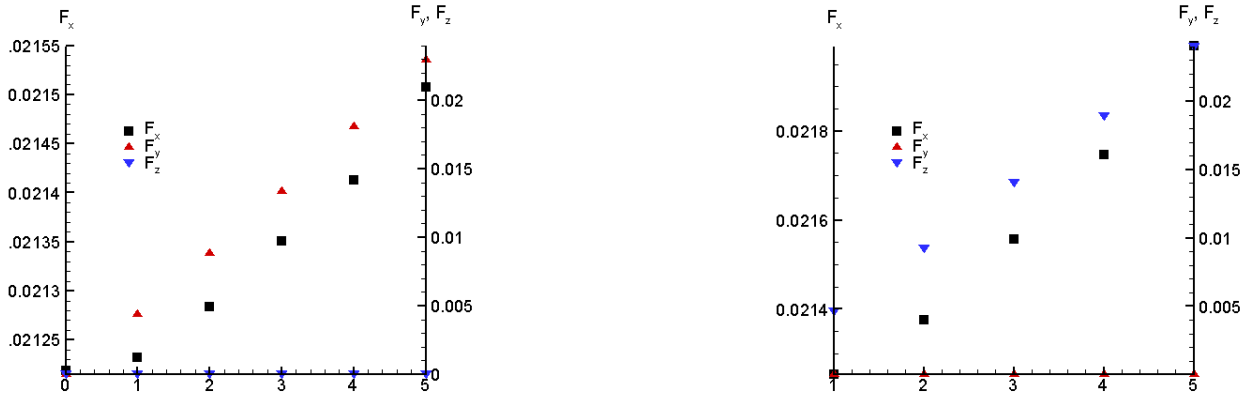

a) Pitch angle effect **b)** Sideslip angle effect

Figure 13. Force coefficient normalized by unit relative area

is the Vehicles Unstructured Solver (AVUS). The approach solves the full Navier-Stokes equations on unstructured meshes, with a cell-centered finite-volume formulation. Inviscid fluxes are evaluated with the exact Riemann solution method of Gottlieb and Groth[23] supplemented with the MUSCL scheme[24] for nominally second order accuracy. Linear variations (gradients) are constructed by a least squares method. Second-order accurate viscous terms are obtained by the MacCormack approach.[25] A point-implicit relaxation method is used for time-integration. Although several turbulence models have been incorporated, only the Spalart-Allmaras model[26] is deployed with this code. Boundary conditions, including those associated with walls, far field and axisymmetry are applied in a standard fashion.[27]

In order to minimize the large resource requirements of these fully viscous solutions, symmetry is invoked. Further, the channel is not considered (see next section). Figure 14a depicts the structure of the mesh employed, which is generated by rotating the axisymmetric mesh by 180 degrees in increments of 2^o, yielding 4.6×10^6 nodes. Figure 14b shows the surface flow in the cone region. The observed pattern is topologically similar in both laminar and turbulent flow. The effect of angle of attack is to impose an inclination in the trajectory, giving rise to a mild accumulation on the leeward plane of symmetry. In the laminar case (not shown), the flow remains unsteady and significant variation is observed in the azimuthal direction. The turning angle increases considerably on the cylinder/isolator segment near the flare juncture where the first shock/boundary layer interaction is encountered. The flowfield near the flare is presently under examination. Although the turbulence modeling issue noted in § D has not been resolved, the solutions indicate that the flow remains separated around the periphery.

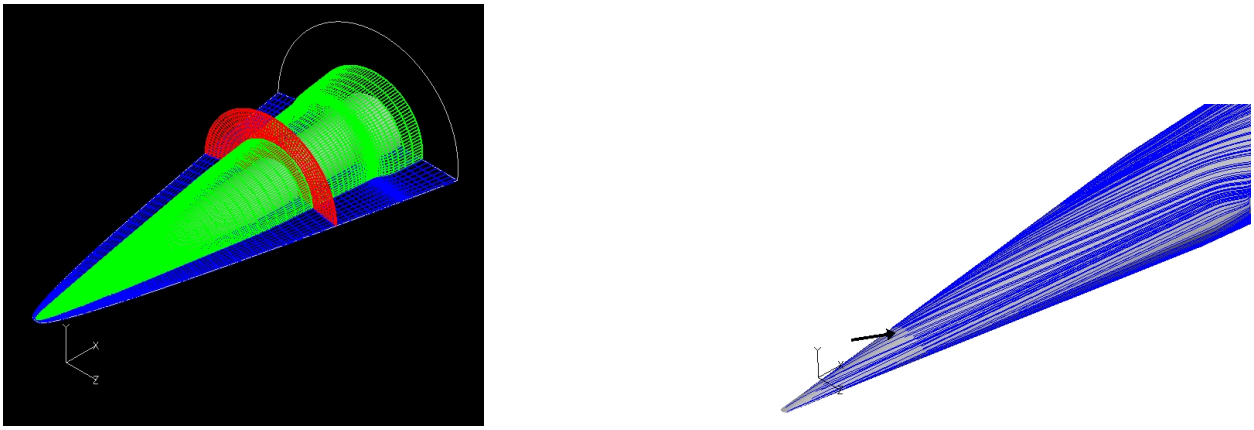

a) Grid structure **b)** Surface oil flow on cone

Figure 14. 3-D simulations at 2 degree angle of attack

B. Viscous Simulations on Test Article

In conjunction with theoretical considerations, the above CFD simulations have served as to determine many of the key parameters of the test article. Each however has restricted attention to specific aspects by invoking suitable assumptions such as axisymmetry or inviscid flow. An effort has also been undertaken to perform viscous simulations on the complete test article. In addition to aiding diagnostic placement, these simulations will ultimately more clearly

identify the influence of the channel on the laminar to turbulent transition and the shock/boundary layer interaction experiments.

The AVUS code is employed for this purpose because of its versatility in treating the complex viscous mesh system required in the channel. Aspects of the grid employed are shown in Fig. 15. A hybrid mesh is employed, comprised of hexahedral and tetrahedral cells . The external flow is discretized with a structured mesh generated by dividing the domain into four blocks (see Fig. 15a). These regions are discretized with 4.5×10^6 points. The mesh generation procedure inside the channel is greatly facilitated by utilizing an unstructured mesh, details of which are shown in Fig. 15b. The interface between the structured and unstructured mesh occurs on the entry and exit planes of the channel, which are treated as internal boundaries of the solver. The number of points in the channel is roughly $18K$ with $86K$ tetrahedral cells and $2.4K$ pyramids.

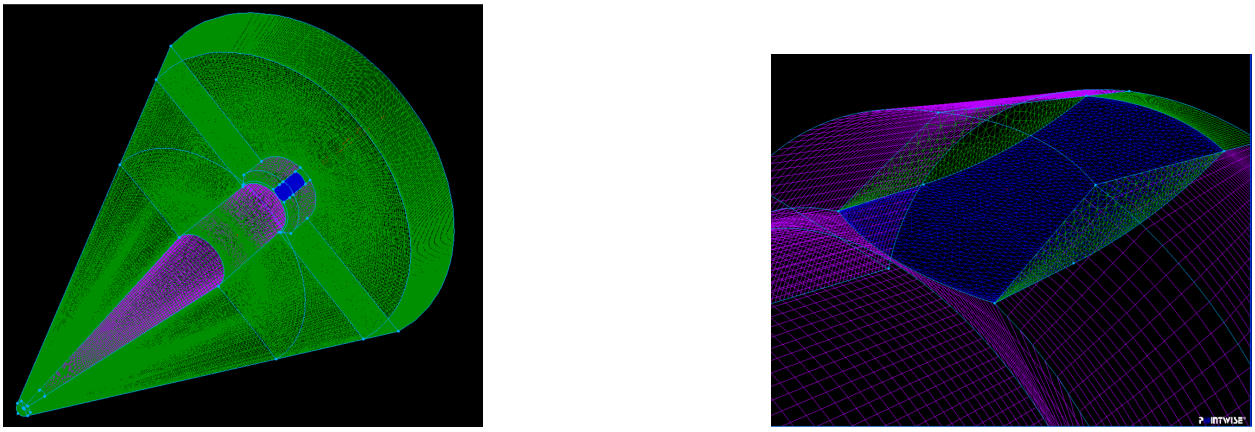

a) Grid - overview **b)** Channel region

Figure 15. Features of mesh employed

Overall aspects of the flow are shown in Fig. 16. The key differences between these and the axisymmetric situation clearly occur in the vicinity of the channel, with the flow on the cone segment being unaffected. The shock generated by the lower surface of the channel is weaker than that associated with the flare face. Consequently the line of separation moves towards the flare juncture near the entrance to the channel. As noted earlier, experimental results suggest that the separated region is considerably larger than predicted with the present model (unmodified Spalart Almaras technique) and relatively coarse mesh. Consequently, the impact of the channel on the plane transverse to it remains to be explored further.

Figure 17 permits a preliminary examination of the flow in the channel. The Mach number is depicted at several cross-flow planes cutting through the channel, together with the heat transfer rate on the surface. The initial cut, taken just upstream of the flare reveals an axisymmetric boundary layer. The trace of the bow shock and the cone/cylinder expansion are also evident. Proceeding downstream, $x = 1.62m$ and $x = 1.65m$, the boundary layers on the flare are modified by the development of the flare shock, while that entering the channel is relatively undisturbed. Channel side-wall boundary layers are formed which grow modestly proceeding downstream, but do not result in choking of the flow. The effect of the shoulder expansion can be observed at $x = 1.69$, where the height of the disturbed region is significantly larger, with the formation of a small non-monotonic Mach gradient region. At the exit plane of the channel, $x = 1.76m$, two pockets of low Mach fluid are observed near the channel walls. These are consistent with the ejection of channel wall boundary layer fluid. The alternate possibility is the ejection of weak corner vortices, though the side-walls of the channel do not generate any significant swept interaction. Simulations with further resolution of the channel region are required to resolve this issue. At the final station plotted, $x = 1.79m$, the external shock profile is similar to that observed with Cart3D (see Fig. 11). Between the shock and the surface, a complex flow structure arises as the lower channel wall boundary layer also undergoes an expansion at the end of the channel. The heat transfer rates plotted on the surface indicate that peak values in this region occur at the sharp trailing edge of the channel, which may be alleviated by suitable smoothing.

The solutions have been employed to provide path-based values of the main flow parameters, density, streamwise velocity, temperature and pressure to aid in the development and analysis of diagnostics for mass capture utilizing line-of-sight principles. The variations along four cross-paths, shown in Fig. 18, have been extracted. For brevity, only values along paths 1 and 4 are shown in Fig. 19 with laminar and turbulent simulations. Many of the anticipated features are evident. The velocity variation is large in the channel side wall boundary layer, but is relatively small in the interior of the channel, even at the downstream location. The pressure rise associated with the relatively mild wave due to the newly developing boundary layer is evident near the edge at Path 1, but extends over most of the interior

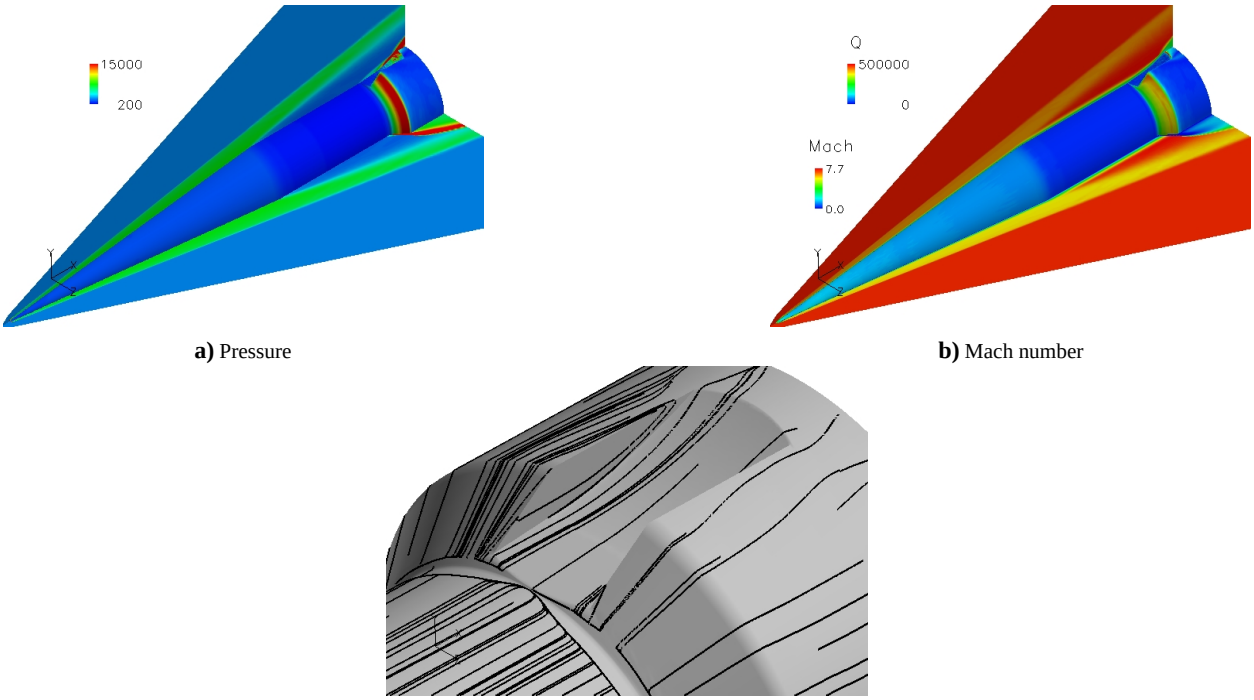

a) Pressure

b) Mach number

c) Surface streamlines near channel

Figure 16. General features of turbulent flow on test article

at path 4. Overall, the effect of turbulent dissipation is to reduce density and increase temperature, especially near the wall.

V. Conclusion

This paper describes a CFD-based strategy to guide development of a flight test article with the goal of obtaining data on fundamental phenomena in hypersonic flow. The primary emphasis is on natural transition under hypersonic conditions (Mach number between 6 and 8) in the relatively quieter environment of flight. A secondary experiment concerns shock/boundary layer interactions, while the tertiary experiment examines the survivability and accuracy of devices to measure mass capture in a pseudo-internal flow. These data will help augment the CFD validation database, analyze peculiarities of and calibrate ground-testing procedures. Combined with semi-empirical and analytical approaches, the evolution of the configuration is traced to the final form, including sequentially a sphere-cone segment followed by a constant radius cylinder to isolate the transition from the other experiments, and a flare whose extent is determined by the base diameter where mating occurs with the booster. Several different codes and techniques are employed to develop the basic configuration, including an unstructured approach (AVUS code), a Cartesian-based (Cart3D) method, a commercial code (GASP) for high-temperature analysis, and a high-fidelity research tool (FDL3DI). Different turbulence models, including the one-equation Spalart Allmaras and two equation $k-\epsilon$ model are employed. This design evolution strategy provides a bound on the parameters likely to be encountered in flight, and permits specifications for measurement gauges, and a framework for pre- and post-flight computational analysis.

Acknowledgements

This effort has benefited greatly from discussions with and guidance from numerous individuals. Extensive assistance was obtained from M. Aftosmis (NASA) on the use of Cart3D. L. Wholey, V. Burnley, G. Brooks, and M. Grismer, all of AFRL, assisted in various aspects of viscous grid generation and use of AVUS. H. Yan (Wright State University) helped in ensuring the proper setup for GASP. All vehicle model data was obtained from D. Adamczak in the form of CFD-friendly CAD models. The authors are also grateful for permission from M. Holden and T. Wadhams to use their experimental data. The work has been sponsored by the Air Force Office of Scientific Research, under tasks monitored by Dr. J. Schmisseur and Dr. F. Fahroo. Computational resources were provided by a grant of computer time from the Department of Defense High Performance Computing Shared Resource Centers at the Army High Performance Computing Research Center (AHPCRC), Naval Oceanographic Office (NAVO), Aeronautical Sciences

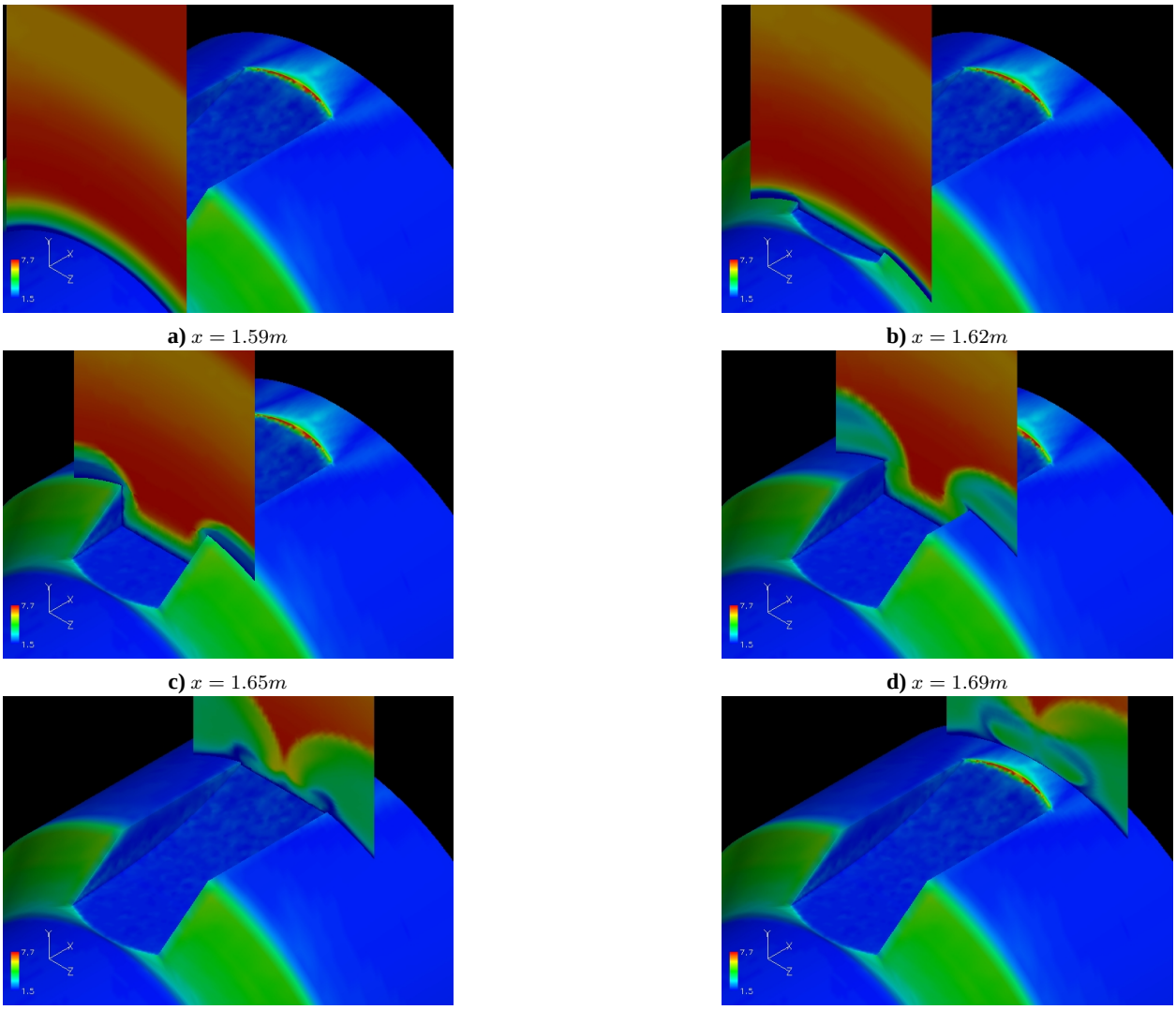

a) $x = 1.59m$ **b)** $x = 1.62m$ **c)** $x = 1.65m$ **d)** $x = 1.69m$ **e)** $x = 1.76m$ **f)** $x = 1.79m$

Figure 17. Structure of flow in channel

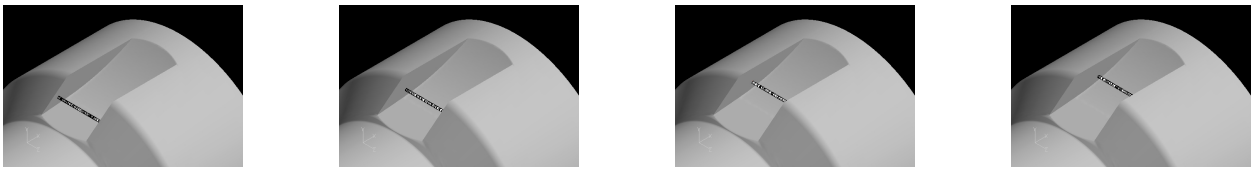

a) Path 1 **b)** Path 2 **c)** Path 3 **d)** Path 4

Figure 18. Paths along which data is extracted

Center (ASC) and the Engineering Research and Development Center (ERDC).

References

[1]Boyce, R., Gerard, S., and Paull, A., "The HyShot scramjet flight experiment - flight data and CFD calculations compared," *AIAA Paper 2003-7029*, 2003.

[2]Kimmel, R., Adamczak, D., Gaitonde, D., Rougeux, A., and Hayes, J., "FRESH FX-1 Boundary Layer Transition Experiment Design," *Submitted for presentation, Aerospace Sciences Exhibit, January 2007*, 2007.

[3]Air Force Research Laboratory, CFD Research Branch, Wright-Patterson AFB, OH, *Air Vehicles Unstructured Solver (AVUS) - User's Manual*.

[4]Gaitonde, D. and Visbal, M., "High-Order Schemes for Navier-Stokes Equations: Algorithm and Implementation into FDL3DI," Tech. Rep. AFRL-VA-WP-TR-1998-3060, Air Force Research Laboratory, Wright-Patterson AFB, 1998.

[5]Aerosoft, Inc., Blacksburg, VA, *GASP Version 4.3 Reference Guide*.

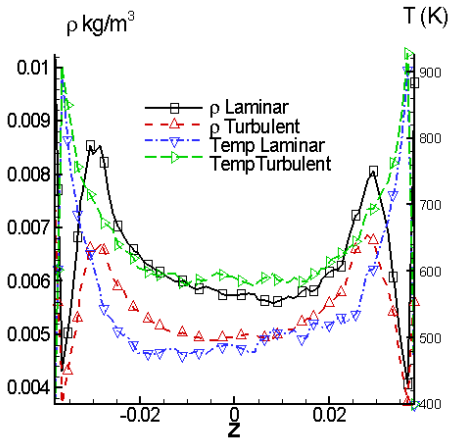

a) Path 1, ρ and T

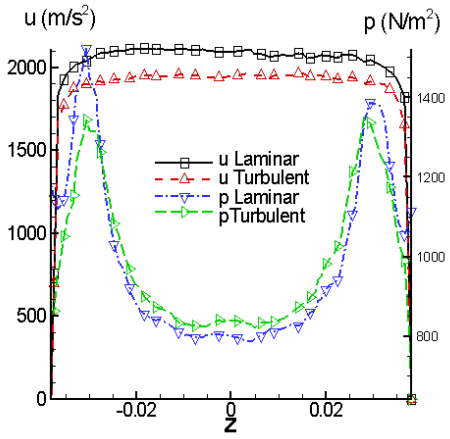

b) Path 1, u and p

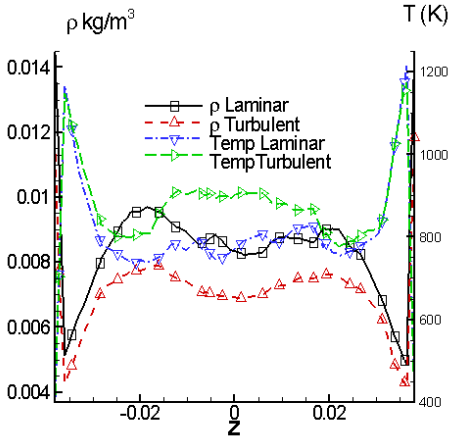

c) Path 4, ρ and T

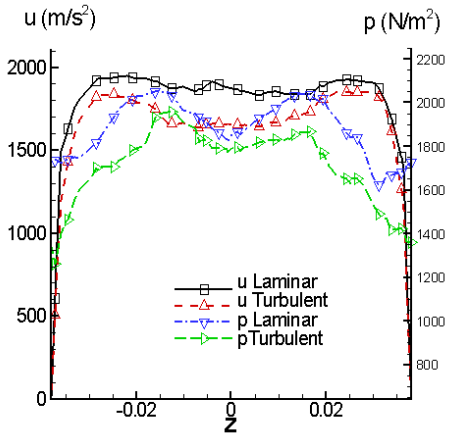

d) Path 4, u and p

Figure 19. Extracted flow profiles in channel

[6]Aftosmis, M., Berger, M., and Alonso, J., "Applications of a Cartesian mesh boundary-layer approach for complex configurations," *AIAA Paper 2006-0652*, 2006.

[7]Schneider, S., "Flight Data for Boundary-Layer Transition at Hypersonic and Supersonic Speeds," *Journal of Spacecraft and Rockets*, Vol. 36, No. 1, Jan-Feb 1999.

[8]Stetson, K. and Kimmel, R., "On Hypersonic Boundary-Layer Stability," *AIAA Paper 92-0737*, 1992.

[9]Liepmann, H. and Roshko, A., *Elements of Gasdynamics*, John Wiley and Sons, Inc., New York, 1963.

[10]Fay, J. and Riddell, F., "Theory of Stagnation Point Heat Transfer Rate in Dissociated Air," *Journal of the Aeronautical Sciences*, Vol. 25, No. 2, 1958.

[11]Holden, M. and Wadhams, T., "Private Communication," , 2006.

[12]Launder, B. and Sharma, B. I., "Application of the Energy Dissipation Model of Turbulence to the Calculation of Flows near a Spinning Disk," *Letters in Heat and Mass Transfer*, Vol. 1, 1974, pp. 131–138.

[13]Sarkar, S., Erlebacher, G., Hussaini, M., and Kreiss, H., "The Analysis and Modelling of Dilational Terms in Compressible Turbulence," *Journal of Fluid Mechanics*, Vol. 227, 1991, pp. 473–493.

[14]Rizzetta, D., "Numerical Simulation of Vortex Induced Oblique Shock-Wave Distortion," *AIAA Paper 96-0039*, Jan. 1996.

[15]Knight, D. and Degrez, G., "Shock Wave Boundary Layer Interactions in High Mach Number Flows – A Critical Survey of Current CFD Prediction Capabilities," Tech. rep., AR-319, Vol. 2, AGARD, 1997.

[16]Mack, L., "Boundary-Layer Stability Theory," Tech. Rep. Part B, Doc. 900-277, JPL, Pasadena, California, May 1969.

[17]Reshotko, E., "Boundary-Layer Stability and Transition," *Annual Review of Fluid Mechanics*, Vol. 8, 1976, pp. 311–349.

[18]Saric, W., Reshotko, E., and Arnal, D., "Hypersonic Laminar-Turbulent Transition," Tech. Rep. AR-319, AGARD, 1998.

[19]Stetson, K., Thompson, E., Donaldson, J., and Siler, L., "Laminar Boundary Layer Stability Experiments on a Cone at Mach 8, Part 2: Blunt Cone," *AIAA Paper 84-0006*, 1984.

[20]Gaitonde, D. and Tumin, A., "Electromagnetic Control of Unstable Disturbances in a Weakly Ionized Entropy Layer," *AIAA Paper 2004-0511*, Jan 2004.

[21]Wang, X. and Zhong, X., "Receptivity of a Mach 8 Flow Over a Sharp Wedge to Wall Blowing-Suction," *AIAA Paper 2005-5025*, 2005.

[22]Zhong, X. and Ma, Y., "Boundary-layer receptivity of Mach 7.99 flow over a blunt cone to free-stream acoustic waves," *J. Fluid Mech.*, Vol. 556, 2006, pp. 55–103.

[23]Gottlieb, J. and Groth, C., "Assessment of Riemann Solvers for Unsteady One-Dimensional Inviscid Flows of Perfect Gases," *J. Comp. Phys.*, Vol. 78, 1988, pp. 437–458.

[24]van Leer, B., "Flux-Vector Splitting For the Euler Equations," Tech. Rep. 82-30, ICASE, September 1982.

[25]MacCormack, R., "The Effect of Viscosity in Hypervelocity Impact Cratering," *AIAA Paper 69-354*, 1969.

[26]Spalart, P. and Allmaras, S., "A One-Equation Turbulence Model for Aerodynamic Flows," *AIAA Paper 92-0439*, Jan. 1992.

[27]Strang, W., Tomaro, R., and Grismer, M., "The Defining Methods of Cobalt60: a Parallel, Implicit Unstructured Euler/Navier-Stokes Flow Solver," *AIAA Paper 99-0786*, 1999.